Boundary-Layer Meteorol (2011) 141:77–92
DOI 10.1007/s10546-011-9630-4

ARTICLE

Computational Fluid Dynamics Modelling of the Diurnal Variation of Flow in a Street Canyon

Kyung-Hwan Kwak · Jong-Jin Baik · Sang-Hyun Lee · Young-Hee Ryu

Received: 1 June 2010 / Accepted: 18 June 2011 / Published online: 12 July 2011

Abstract Urban surface and radiation processes are incorporated into a computational fluid dynamics (CFD) model to investigate the diurnal variation of flow in a street canyon with an aspect ratio of 1. The developed CFD model predicts surface and substrate temperatures of the roof, walls, and road. One-day simulations are performed with various ambient wind speeds of 2, 3, 4, 5, and 6 $\mathrm{m\,s^{-1}}$, with the ambient wind perpendicular to the north–south oriented canyon. During the day, the largest maximum surface temperature for all surfaces is found at the road surface for an ambient wind speed of 3 $\mathrm{m\,s^{-1}}$ (56.0°C). Two flow regimes are identified by the vortex configuration in the street canyon. Flow regime I is characterized by a primary vortex. Flow regime II is characterized by two counter-rotating vortices, which appears in the presence of strong downwind building-wall heating. Air temperature is relatively low near the downwind building wall in flow regime I and inside the upper vortex in flow regime II. In flow regime II, the upper vortex expands with increasing ambient wind speed, thus enlarging the extent of cool air within the canyon. The canyon wind speed in flow regime II is proportional to the ambient wind speed, but that in flow regime I is not. For weak ambient winds, the dependency of surface sensible heat flux on the ambient wind speed is found to play an essential role in determining the relationship between canyon wind speed and ambient wind speed.

Keywords Computational fluid dynamics model · Diurnal variation · Flow regime · Street-canyon flow · Urban radiation process · Urban surface process

K.-H. Kwak · J.-J. Baik (✉) · S.-H. Lee · Y.-H. Ryu
School of Earth and Environmental Sciences, Seoul National University,
599 Gwanak-ro, Gwanak-gu, Seoul 151-742, Republic of Korea
e-mail: jjbaik@snu.ac.kr

Present Address:
S.-H. Lee
Earth and Environmental Sciences Division, Los Alamos National Laboratory, Los Alamos, NM, USA

1 Introduction

Street-canyon flow has received much attention because of its importance in many urban environmental and planning problems as well as its fluid dynamical interest. Many studies of street-canyon flow under isothermal conditions have concentrated on flow patterns in terms of the canyon aspect ratio (H/W, where H is the building height and W is the street width), building configuration, and ambient wind speed and direction (Li et al. 2006). Recently, more attention has been paid to the impact of thermal forcing on street-canyon flow. Field measurements have shown the temporal variation of street-canyon flow with a diurnal solar cycle (Nakamura and Oke 1988; Louka et al. 2002; Eliasson et al. 2006; Offerle et al. 2007; Idczak et al. 2007). Laboratory experiments (Uehara et al. 2000; Kovar-Panskus et al. 2002) and two-dimensional numerical experiments (Sini et al. 1996; Kim and Baik 1999, 2001; Xie et al. 2005; Cheng et al. 2009) were performed to examine the effects of solar heating on street-canyon flow. Sini et al. (1996) found that when H/W is 0.89, the downwind building-wall heating divides a primary vortex into two counter-rotating vortices, whereas the ground or the upwind building-wall heating enhances vortex circulation in a street canyon. Kim and Baik (1999) demonstrated that two or three vortices can be formed in a street canyon depending on the differential surface heating (no heating, upwind building-wall heating, street-canyon bottom heating, and downwind building-wall heating) and canyon aspect ratio. Kim and Baik (2001) classified street-canyon flow into five flow regimes in terms of canyon aspect ratio and the degree of street-canyon bottom heating. Kovar-Panskus et al. (2002) performed a wind-tunnel study with $H/W = 1$ to examine how the windward-facing wall heating changes the in-canyon flow pattern. The study showed that as the Froude number (Fr) decreases below 1, a primary vortex weakens and relatively stagnant flow appears in a lower region. Xie et al. (2005) quantified the relative contributions of mechanical and thermal forcings to flow features in the case of $H/W = 1$ using Gr/Re^2, where Gr is the Grashof number and Re is the Reynolds number. Numerical experiments have shown that when the bottom surface is heated, the street-canyon flow pattern in three dimensions is different from that in two dimensions (Tsai et al. 2005; Baik et al. 2007; Kang et al. 2008). In three dimensions, a primary vortex in a street canyon meanders in the along-canyon direction as well as in the cross-canyon direction. In most numerical studies, the surface heating, which was represented by a temperature difference between the surfaces and adjacent air, was prescribed as a constant value with time. A few studies incorporated radiation and heat transfer processes into numerical models to examine steady-state flow in the vicinity of buildings (Chen et al. 2004; Hadavand et al. 2008).

Our study aims to develop a computational fluid dynamics (CFD) model that includes urban surface and radiation processes and to investigate the diurnal variation of street-canyon flow using the CFD model. The urban surface and radiation model that is a part of an urban canopy model is used to calculate the surface temperatures of the roof, walls, and road prognostically. In Sect. 2, a CFD model is described, and is validated in Sect. 3. Simulation results are presented and discussed in Sect. 4, with a summary and conclusions given in Sect. 5.

2 Numerical Model

For this study, the urban surface and radiation model that is a part of the urban canopy model developed by Ryu et al. (2011) is incorporated into the CFD model developed by Kim and Baik (2004) and Baik et al. (2007). The CFD model is a Reynolds-averaged Navier–Stokes equations (RANS) model with the renormalization group (RNG) k–ε

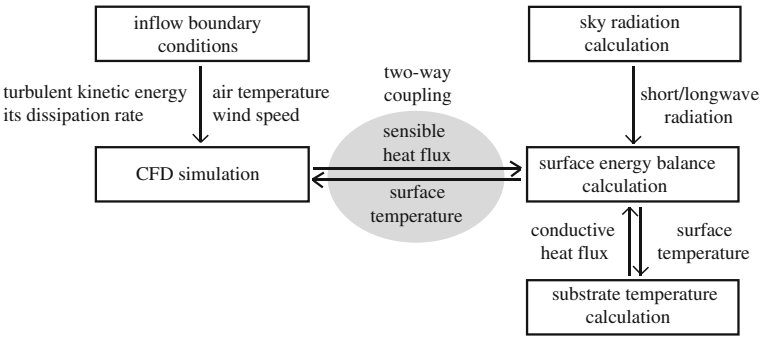

Fig. 1 Flow chart of two-way coupling between the urban surface and radiation model and the CFD model

turbulence closure scheme. Figure 1 shows the flow chart of two-way coupling between the urban surface and radiation model and the CFD model. The urban surface and radiation model predicts surface and substrate temperatures of the roof, walls, and road, with the predicted surface temperatures used as a thermal boundary condition for the CFD model. The CFD model calculates sensible heat fluxes from the roof, walls, and road using a wall function. Since the surface temperature and sensible heat flux are regarded as representative values for a surface in the surface energy balance equation, sensible heat fluxes calculated at individual grid points in the CFD model are averaged over the surface.

Surface and substrate temperatures are obtained by the heat diffusion equation and the heat conduction equation, using

$$C_i \frac{\partial T_i}{\partial t} = -\frac{\partial F_i}{\partial z_p}, \tag{1}$$

$$F_i = -k_i \frac{\partial T_i}{\partial z_\mathrm{p}}, \tag{2}$$

where T_i is the temperature, F_i is the conductive heat flux, C_i is the volumetric heat capacity, k_i is the thermal conductivity, and z_p is the coordinate in the direction perpendicular to the surface. The subscript i indicates each surface.

The surface boundary condition of Eq. (1) is given by the surface energy balance equation,

$$F_i = S_i^{\uparrow\downarrow} + L_i^{\uparrow\downarrow} - H_i, \tag{3}$$

where $S_i^{\uparrow\downarrow}$, $L_i^{\uparrow\downarrow}$, and H_i are the net shortwave radiative flux, the net longwave radiative flux, and the sensible heat flux for each surface i, respectively. For given time (in local standard time, LST) and location (in longitude and latitude), the direct (S_dir) and diffuse (S_diff) components of downward shortwave radiative flux at the reference height are estimated following the method of Panão et al. (2007)

$$S_\mathrm{dir} = K_\perp \cos\phi_\mathrm{z}, \tag{4}$$

$$S_\mathrm{diff} = G - S_\mathrm{dir}, \tag{5}$$

where $K_\perp$ and G are the normal and global direct irradiances, respectively. Here, the solar zenith angle ϕ_z is used to quantify S_dir and G. The downward longwave radiative flux (L_atm) is estimated following Swinbank (1963) and Lee and Park (2008), viz.

$$L_{\mathrm{atm}} = 9.4 \times 10^{-6} \sigma T_{\mathrm{atm}}^{6}, \tag{6}$$

where σ is the Stefan–Boltzmann constant. Note that L_{atm} in Eq. (6) is only a function of the atmospheric temperature (T_{atm}).

Sky radiation consists of direct and diffuse shortwave radiation and longwave radiation. A method of partitioning the sky radiation into net shortwave/longwave radiation at each surface is the same as that of Ryu et al. (2011). Unlike diffuse shortwave radiation and longwave radiation that are isotropic, direct shortwave radiation has a single direction, differentiating a sunlit surface from a shaded surface. In definition, a sunlit surface receives non-zero direct shortwave radiation somewhere at the surface, whereas a shaded surface receives no direct shortwave radiation anywhere at the surface. A sunlit surface in a street canyon is determined by the solar azimuth angle, canyon orientation, solar zenith angle, and canyon aspect ratio. Radiation incident into the canyon is allowed to reflect upon the walls and road three times for shortwave radiation and once for longwave radiation. The final reflected radiation is totally absorbed by each surface to conserve total radiative energy.

Following the method of Versteeg and Malalasekera (1995), the surface sensible heat flux (h_i) at a grid point is calculated using the wall function in the CFD model

$$h_i = -\rho C_{\mathrm{p}} C_{\mu}^{\frac{1}{4}} k_{\mathrm{a}}^{\frac{1}{2}} \frac{T_{\mathrm{a}} - T_i}{T^{+}}, \tag{7}$$

where ρ is the air density, C_{p} is the specific heat of air at constant pressure, k_{a} and T_{a} are the turbulent kinetic energy and the air temperature at the nearest grid point to the surface, respectively, and T^{+} is the universal temperature distribution for near-surface turbulent flows. C_{μ} ($= 0.0845$) is a constant. The universal temperature distribution requires roughness lengths. Harman and Belcher (2006) suggested that the roughness length for momentum is ten times larger than that for heat. Following their suggestion, we use 0.05 and 0.005 m as roughness lengths for momentum and heat, respectively.

3 Model Validation

The RANS model was validated using the wind-tunnel dataset (Baik et al. 2007). Another part of the coupled CFD model, the urban surface and radiation model, is validated using the field dataset from Guerville, France (1.44°E, 48.56°N) for 28 July 2004 (Idczak et al. 2007, 2010). The 1:5 scale street canyon has an aspect ratio of 2.48 with a width of 2.1 m and a north-east to south-west orientation (54° from due north). Observed shortwave radiation, longwave radiation, and ambient air temperature are used as meteorological forcings for the CFD model. Wind speed and direction at the inflow boundary are set to 2 $\mathrm{m\,s^{-1}}$ and south-easterly (75° from the canyon axis), respectively, which are similar to those measured at the top of a 10-m mast in the daytime. The values of physical properties of surface materials from Idczak et al. (2010) are used.

Figure 2 shows the simulated and observed surface temperatures of the northern wall, southern wall, and ground for the day. The CFD model well simulates two peaks of the surface temperatures for two opposite walls; a primary peak is caused by direct shortwave radiation and a secondary peak is caused by reflected shortwave radiation from the opposite wall. The wall temperatures are slightly underestimated, whereas the ground temperature is overestimated in the late afternoon. The maximum difference between the observed and simulated surface temperatures is 2.3°C (1610 LST) at the northern wall, 4.5°C (1140 LST) at the southern wall, and 3.2°C (1740 LST) at the ground. In general, however, the diurnal

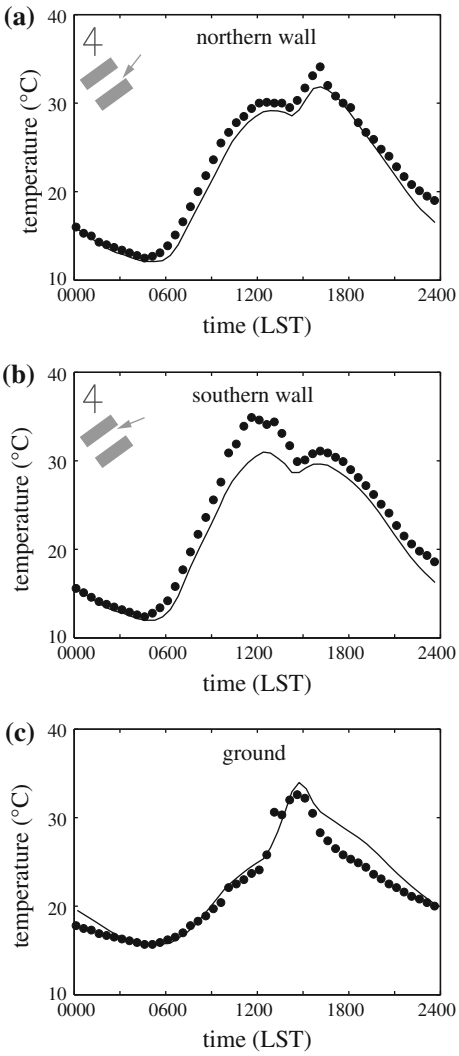

Fig. 2 Diurnal variations of observed (*mark*) and simulated (*line*) surface temperatures of **a** northern wall, **b** southern wall, and **c** ground

variations of simulated surface temperatures are in good agreement with those observed. This indicates that the urban surface and radiation model is suitable for coupling with the RANS model for an investigation of the diurnal variation of street-canyon flow with realistically varying surface temperatures.

Surface temperature directly interacts with the surface sensible heat flux that is calculated using a wall function in the CFD model. In Eq. (7), T_a and T^+ are associated with an interval of grid nearest to a surface. To test whether the grid intervals of 0.3 m in this section and 0.5 m in Sect. 4 are reasonable choices, we performed simulations with different grid intervals and compared simulated surface temperatures to those observed in the 1:5 scale street canyon. In these simulations, the interval of grid nearest to a surface is varied with 0.05, 0.1, 0.15, 0.2, 0.3, 0.5, 0.7, 0.9, and 1.0 m while other grid intervals in a computational domain are the same as those in the validation case. It was found that the simulated surface temperatures (also

simulated sensible heat fluxes) with the grid intervals of 0.15, 0.2, 0.3, 0.5, 0.7, and 0.9 m are very similar to one another and well matched with the observed temperatures. Therefore, it is appropriate to use a wall function with the grid intervals of 0.3 and 0.5 m for calculating surface temperature and sensible heat flux.

4 Results and Discussion

4.1 Model Set-up

Figure 3 depicts the computational domain and building configuration. Buildings and a street canyon are aligned in the y-direction (north–south direction) and infinitely long. Both the building height and street canyon width are 20 m, giving a canyon aspect ratio of 1. The domain size is 40 m in the x-direction (east–west direction), 50 m in the y-direction, and 60.1 m in the z-direction. The grid interval is 0.5 m in the x-direction and 1 m in the y-direction. In the vertical, the grid interval is 0.5 m up to $z = 32$ m and then gradually increases with an expansion ratio of 1.1. The CFD model is integrated for 24 h with a timestep of 0.1 s. The easterly ambient (inflow) wind is perpendicular to the along-canyon direction above the roof level. The ambient wind speed (U_{amb}) is constant with height, and five different ambient wind speeds of 2, 3, 4, 5, and 6 m s^{-1} are considered. Cyclic boundary conditions are applied at the spanwise boundaries (y-direction), while zero gradient boundary conditions are applied at the outflow and upper boundaries. Four surfaces (roof, upwind building wall, downwind building wall, and road) have their own thermal properties: surface albedos and emissivities, thermal conductivities, and heat capacities following those of the Marseille case summarized

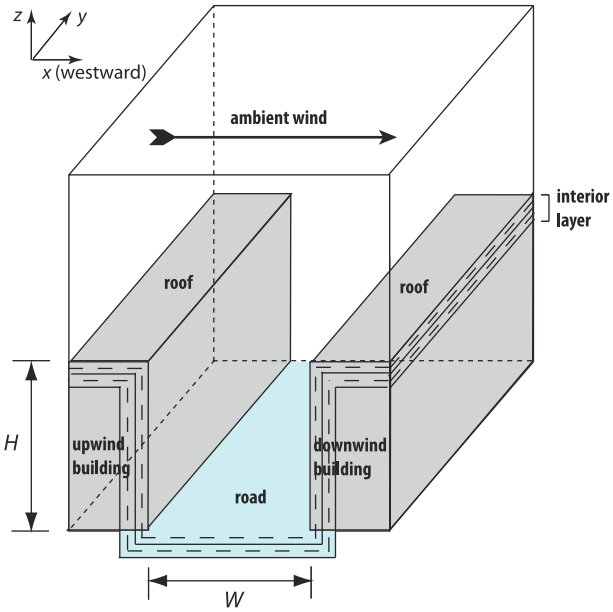

Fig. 3 Computational domain and building configuration. H is the building height and W is the street canyon width. Positive on the x-axis is westward

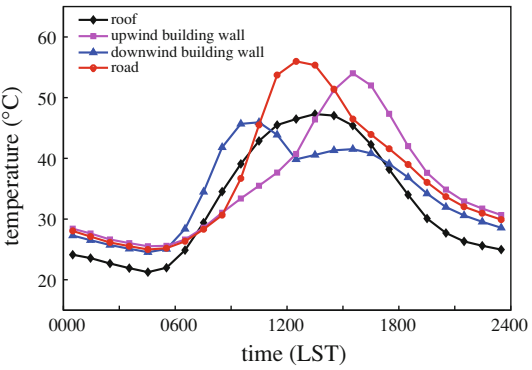

Fig. 4 Diurnal variations of the surface temperatures of roof (*diamond*), upwind building wall (*square*), downwind building wall (*triangle*), and road (*circle*) in the control simulation. Surface temperatures are hourly averaged

by Lee and Park (2008). The substrate of roof, walls, and road is comprised of 20 layers having a depth of 0.4 m. At the bottom of the innermost layer, a zero-flux boundary condition is applied. A 24-h spin-up time is allowed to obtain substrate temperatures that are used as initial conditions.

One-day simulations are performed for 18 June 2007 in Seoul, Korea, a day that was clear and hot. The hourly air temperatures observed at the Korea Meteorological Observatory (126.97°E, 37.55°N) are used as ambient (inflow) air temperatures with a time interpolation. The observation showed a maximum air temperature of 32.7°C at 1500 LST and a minimum air temperature of 20.6°C at 0600 LST. Sunrise was at 0445 LST with sunset at 1915 LST.

4.2 Control Simulation

To investigate the effects of surface heating by sky radiation on street-canyon flow, the case with an ambient wind speed of 3 $\mathrm{m\,s^{-1}}$ is selected as a control simulation. During the day, the upwind building wall from 1200 to 1915 LST, the downwind building wall from 0445 to 1200 LST, and the road from 0840 to 1520 LST are the sunlit surfaces. The roof is always the sunlit surface in the daytime. Figure 4 shows the diurnal variations of surface temperatures in the control simulation. The maximum temperature at each surface is 47.3°C at 1330 LST (roof), 54.0°C at 1530 LST (upwind building wall), 45.9°C at 1030 LST (downwind building wall), and 56.0°C at 1230 LST (road). It is interesting that a secondary peak in the downwind building-wall temperature (41.5°C at 1530 LST) appears when the upwind building-wall temperature shows the maximum. The strongly heated surface also raises adjacent surface temperatures through longwave radiation emitted from the heated surface, thus forming the secondary peak. The radiation trapping effect in the street canyon is caused not only by emitted longwave radiation but also by reflected shortwave radiation. The road surface temperature is higher than the roof surface temperature around their peak times. This is partly due to the radiation trapping effect, together with a low albedo (0.08) of the road. In the nighttime, the roof has the lowest surface temperature among the surfaces. This is related to the radiation trapping effect, which delays decreases in the surface temperatures of the walls and the road.

The diurnal variations of surface sensible heat fluxes are shown in Fig. 5. The maximum sensible heat flux from each surface is 476 $\mathrm{W\,m^{-2}}$ at 1230 LST (roof), 163 $\mathrm{W\,m^{-2}}$ at 1530 LST (upwind building wall), 145 $\mathrm{W\,m^{-2}}$ at 0930 LST (downwind building wall), and 374 $\mathrm{W\,m^{-2}}$ at 1230 LST (road). In the daytime, the sensible heat flux is larger from the roof than from the road, although the road surface temperature is higher than the roof surface

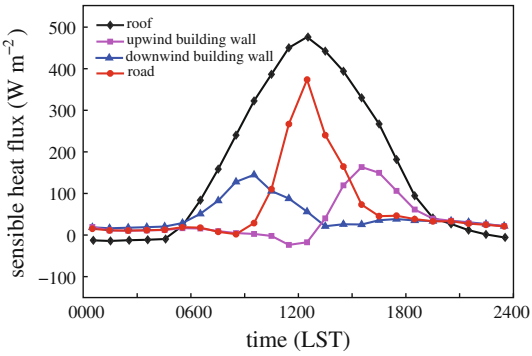

Fig. 5 Diurnal variations of sensible heat fluxes from roof (*diamond*), upwind building wall (*square*), downwind building wall (*triangle*), and road (*circle*) in the control simulation. Surface sensible heat fluxes are hourly averaged

temperature except in the early morning. Here, a higher canyon-air temperature than the ambient air temperature plays a key role in reducing sensible heat fluxes from the walls and the road because the surface sensible heat flux is proportional to the temperature difference between a surface and the adjacent air. In the nighttime, sensible heat fluxes from the surfaces in the street canyon remain positive because of storage heat release. This storage heat in the nighttime is a consequence of the large thermal inertia of the surfaces in the street canyon. A larger surface sensible heat flux implies a stronger thermal effect on street-canyon flow since it strengthens buoyancy force in the vicinity of the strongly heated surface. Therefore, the diurnal variation of street-canyon flow is strongly associated with that of the surface sensible heat flux.

Figure 6 shows along-canyon averaged streamline fields in 1-h intervals from 0400 LST to 1500 LST. Streamline fields during the night before 0400 LST and in the afternoon after 1500 LST are almost the same as those at 0400 (Fig. 6a) and 1500 LST (Fig. 6l), respectively. A clockwise-rotating primary vortex, which is mechanically induced, forms in the street canyon at 0400, 0500, and 0600 LST (Fig. 6a–c). At these times, the canyon-averaged mean kinetic energy (a half of the canyon-averaged square velocity) is about 0.16 $m^2\ s^{-2}$. After the sun rises at 0445 LST, the sensible heat flux from the downwind building wall becomes larger than that from the upwind building wall and road. The downwind building-wall heating perturbs the primary vortex (Fig. 6d). At 0800 LST, two counter-rotating vortices appear, which are the clockwise-rotating primary vortex remaining in the upper part and the counterclockwise-rotating secondary vortex growing in the lower part (Fig. 6e). The lower vortex circulation interferes with the upper vortex circulation, so that the canyon-averaged mean kinetic energy decreases to 0.054 $m^2\ s^{-2}$ at 0820 LST. The road heating by direct shortwave radiation that starts from 0840 LST strengthens the lower vortex circulation. As the sensible heat flux from the road becomes larger, the mechanically induced upper vortex shrinks from 0900 to 1100 LST (Fig. 6f–h) with increasing canyon-averaged mean kinetic energy from 0.063 $m^2\ s^{-2}$ at 0900 LST to 0.186 $m^2\ s^{-2}$ at 1100 LST. After the sensible heat flux from the road becomes larger than that from the downwind building wall, the two counter-rotating vortices have difficulty in sustaining themselves and are abruptly merged into a single primary vortex again (Fig. 6i). The road heating strengthens the primary vortex circulation and increases the canyon-averaged mean kinetic energy, which is 1.09 $m^2\ s^{-2}$ at 1145 LST (daily maximum value). In the afternoon, the upwind building-wall heating increases the sensible heat flux from the wall, whereas the sensible heat flux from the road decreases. Then, the canyon-averaged mean kinetic energy decreases. The vortex shape changes very little in the afternoon (Fig. 6j–l).

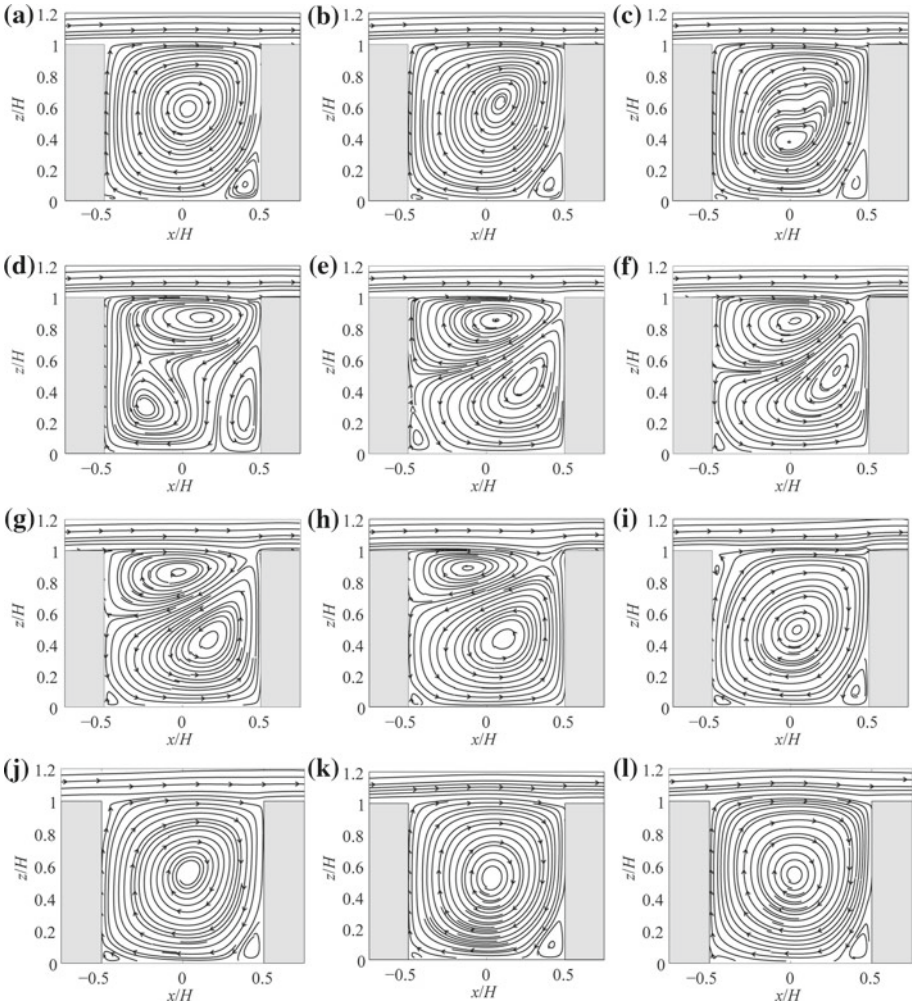

Fig. 6 Along-canyon averaged streamline fields at **a** 0400, **b** 0500, **c** 0600, **d** 0700, **e** 0800, **f** 0900, **g** 1000, **h** 1100, **i** 1200, **j** 1300, **k** 1400, and **l** 1500 LST in the control simulation. The along-canyon average is taken from $y/H = -1.25$ to 1.25

Based upon the analysis of the diurnal variation of the street-canyon flow, two flow regimes are identified. Flow regime I is characterized by a primary vortex shown at 0400, 0500, 0600, 1200, 1300, 1400, and 1500 LST in Fig. 6. This flow regime appears with road and/or upwind building-wall heating as well as no surface heating. Flow regime II is characterized by two counter-rotating vortices consisting of a mechanically driven upper vortex and a thermally driven lower vortex. This flow regime appears at 0800, 0900, 1000, and 1100 LST in Fig. 6 when the downwind building wall is strongly heated. In the control simulation, the regime transitions from I to II and from II to I occur at 0700 and 1130 LST, respectively. A streamline field at 0700 LST (Fig. 6d) represents a transition of the flow regime. The transition time of the flow regimes depends on ambient wind speed and differential sensible heat fluxes between the walls and road (not shown here).

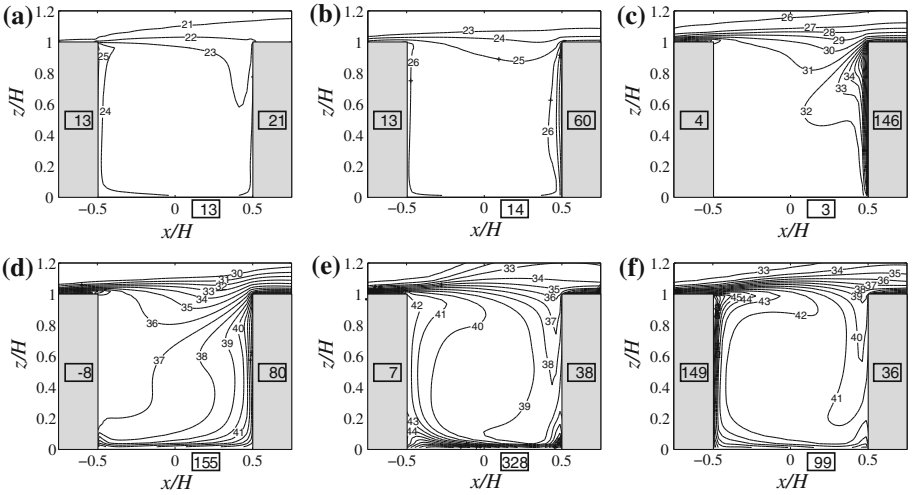

Fig. 7 Along-canyon averaged temperature fields at **a** 0500, **b** 0700, **c** 0900, **d** 1100, **e** 1300, and **f** 1500 LST in the control simulation. The contour interval is 1°C. The values in the *boxes* indicate the area-averaged sensible heat fluxes from surfaces in $\mathrm{W\,m^{-2}}$

Figure 7 shows along-canyon averaged temperature fields at 0500, 0700, 0900, 1100, 1300, and 1500 LST. When the downwind building-wall heating is insignificant in the early morning (Fig. 7a, b), the temperature fields in the street canyon are relatively uniform. Since the canyon-air temperature is higher than the air temperature above the roof level, the entrance region of ambient air into the street canyon, located near the roof of the downwind building, coincides with the low temperature region in the canyon. In flow regime II, the temperature field changes in accordance with the locations of two counter-rotating vortices (Fig. 7c, d). Cool ambient air mostly flows into the upper vortex, whereas heated air near the downwind building wall tends to remain in the lower vortex. Thus, the spatial extent of high/low temperature regions expands/shrinks as the downwind building-wall heating increases. The temperature field changes remarkably when the transition from flow regime II to flow regime I occurs (i.e., from Fig. 7d to Fig. 7e). After the transition occurs, the region of cool/warm air appears along the downwind/upwind building wall, following the clockwise vortex circulation in flow regime I (Fig. 7e, f).

4.3 Simulations with Various Ambient Wind Speeds

Figure 8 shows along-canyon averaged streamline fields at 0800, 0900, and 1000 LST for ambient wind speeds of 2, 4, and $6\,\mathrm{m\,s^{-1}}$. As the ambient wind speed increases from 2 to $6\,\mathrm{m\,s^{-1}}$, it is clear in flow regime II that a mechanically driven upper vortex expands, whereas a thermally driven lower vortex shrinks. A slope of margin between the two vortices also changes. The slope is less steep with increasing ambient wind speed. When the ambient wind speed is $2\,\mathrm{m\,s^{-1}}$, the lower vortex reaches the roof level near the downwind building. Hence, heat can be directly exchanged across the roof level (Fig. 8a–c). When the ambient wind speeds are 4 (Fig. 8d–f) and $6\,\mathrm{m\,s^{-1}}$ (Fig. 8g–i), on the other hand, there is downward motion near the upper part of the downwind building. Therefore, the downward motion enhanced by the strong ambient wind plays an important role in enlarging the upper vortex and reducing the slope of margin between the two vortices.

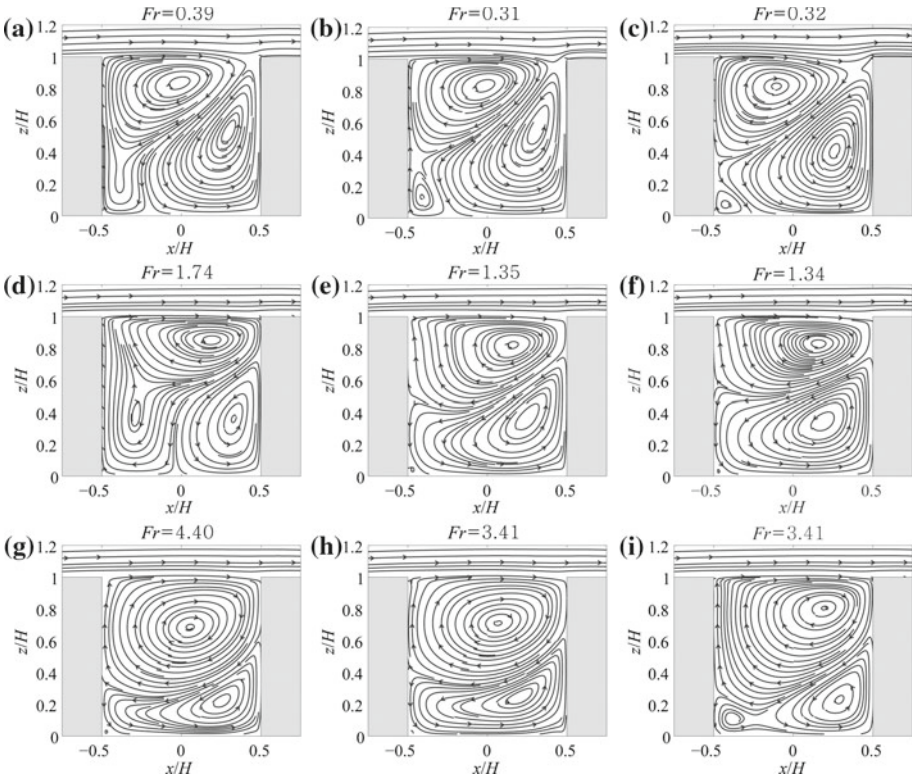

Fig. 8 Along-canyon averaged streamline fields at **a** 0800, **b** 0900, and **c** 1000 LST for an ambient wind speed of 2 m s^{-1}, at **d** 0800, **e** 0900, and **f** 1000 LST for an ambient wind speed of 4 m s^{-1}, and at **g** 0800, **h** 0900, and **i** 1000 LST for an ambient wind speed of 6 m s^{-1}. The values of the Froude number are given

Flow fields in Fig. 8 are compared to those in the wind-tunnel study of Kovar-Panskus et al. (2002). For this, the Froude number defined as $Fr = U_{\mathrm{amb}}^2 T_{\mathrm{amb}} / gH(T_i - T_{\mathrm{amb}})$ is introduced, where T_{amb} is the ambient air temperature, g is the gravitational acceleration, and T_i is the downwind building-wall temperature. Since the downwind building-wall temperature is little changed by the ambient wind speed, Fr decreases with decreasing ambient wind speed. Fr is lower at 0900 and 1000 LST than at 0800 LST according to the variation of the downwind building-wall temperature (see Fig. 4). As Fr decreases, the upper vortex shrinks and moves upward. This is consistent with the wind-tunnel result of Kovar-Panskus et al. (2002). Different flow patterns between our simulations and the wind-tunnel experiments for similar Fr might be caused to some extent by the temperature differences of other surfaces.

Figure 9 shows the areal (xy-plane) and hourly averaged vertical profiles of canyon-air temperatures in 0800–0900 (flow regime II) and 1500–1600 LST (flow regime I). In flow regime II, the vertical temperature profiles reflect the extent of the upper vortex. As the ambient wind speed increases, the vertical level of the highest air temperature is lowered due to the expansion of the upper vortex. In flow regime I, the canyon-air temperature does not vary significantly with height except near the street bottom and roof level. As the ambient wind speed increases, the canyon-averaged air temperature decreases because heat exchange across the roof level becomes large. When the ambient wind speed is 2 m s^{-1}, canyon vortices

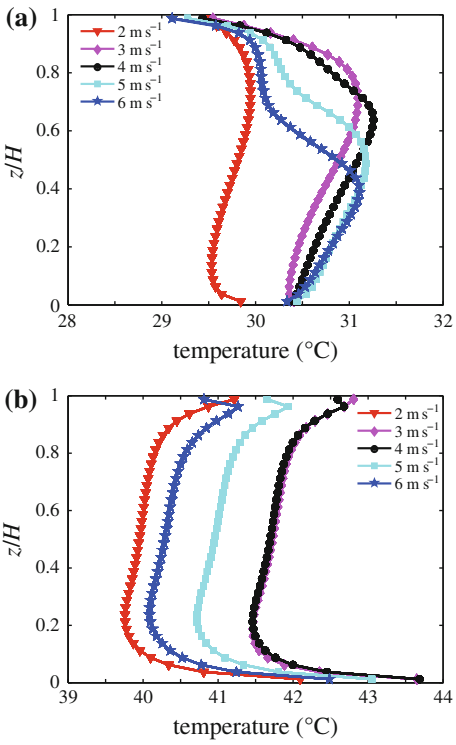

Fig. 9 Vertical profiles of areal and hourly averaged canyon-air temperatures in **a** 0800–0900 LST and **b** 1500–1600 LST for ambient wind speeds of 2, 3, 4, 5, and 6 m s^{-1}

are not completely isolated from the ambient flow, allowing the active interaction of canyon air with ambient air across the roof level in both flow regimes.

Relationships between canyon wind speed and ambient wind speed can be found in previous studies. Nakamura and Oke (1988) suggested an approximately linear relationship between canyon wind speed and ambient wind speed. Santamouris et al. (1999) argued that canyon wind speed is not directly related to ambient wind speed because not only a mechanical influence but also a thermal influence is important in the canyon circulation for weak ambient winds.

We examine the relationship between canyon wind speed and ambient wind speed in two flow regimes. Figure 10 shows the variations of mean canyon wind speed (U_{can}) and normalized canyon wind speed ($K = U_{can}/U_{amb}$) with the ambient wind speed. The mean canyon wind speed is defined and calculated as the root-mean-square velocity in the street canyon. The dependencies of K on the ambient wind speed are different in the two flow regimes (Fig. 10b). In 1500–1600 LST (flow regime I), K decreases with increasing ambient wind speed because the mean canyon wind speed is large even for weak ambient winds (e.g., 2 and 3 m s^{-1}). The mean canyon wind speed is not proportional to the ambient wind speed. In 0800–0900 LST (flow regime II), on the other hand, K does not change much between 0.1 and 0.2 with the ambient wind speed, showing a linear relationship between mean canyon wind speed and ambient wind speed. This linear relationship is in agreement with Nakamura and Oke (1988). For strong ambient winds (e.g., 5 and 6 m s^{-1}), K is approximately 0.2 regardless of flow regime. For weak ambient winds (e.g., 2 and 3 m s^{-1}), however, K significantly deviates from 0.2 in flow regime I because a thermal influence as well as a mechanical influence becomes important as mentioned in Santamouris et al. (1999).

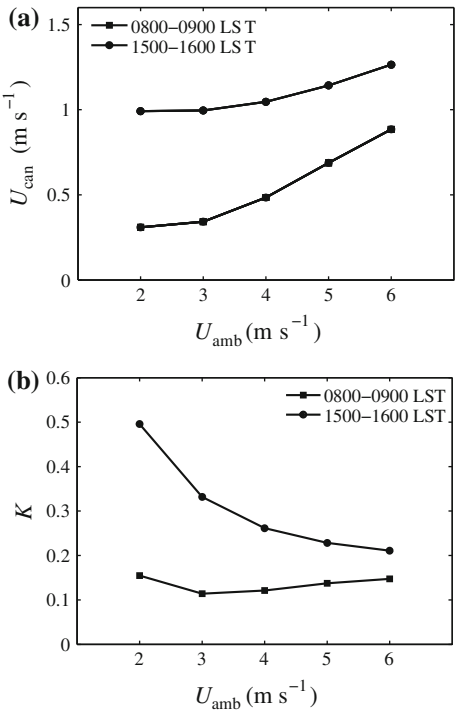

Fig. 10 Variations of **a** mean canyon wind speed (U_{can}) and **b** normalized canyon wind speed (K) in 0800–0900 LST (*square*) and 1500–1600 LST (*circle*) with ambient wind speed

The difference in the dependencies of K on the ambient wind speed for the two flow regimes implies that differential sensible heat fluxes from the surfaces play an important role in strengthening and weakening street-canyon flow, especially for weak ambient winds. To confirm this, the dependencies of sensible heat fluxes from the walls on the ambient wind speed are examined (Fig. 11a). In 1500–1600 LST (flow regime I), the sensible heat flux from the upwind building wall remains almost constant between 165 and 171 W m^{-2} regardless of the ambient wind speed, except in the case of an ambient wind speed of 6 m s^{-1}. In 0800–0900 LST (flow regime II), on the other hand, the sensible heat flux from the downwind building wall increases from 128 (3 m s^{-1}) to 179 W m^{-2} (6 m s^{-1}) with increasing ambient wind speed, except in the case of an ambient wind speed of 2 m s^{-1}. In both periods, the sensible heat fluxes from the road do not significantly vary with the ambient wind speed (not shown here). As mentioned in Sect. 2, the surface sensible heat flux depends on the turbulent kinetic energy and the temperature difference between a surface and the adjacent air. The temperature difference between a wall and air determines the magnitude of the sensible heat flux from the wall but does not strongly depend on the ambient wind speed for all cases as shown in Fig. 11b. However, the root of the turbulent kinetic energy shows a strong dependency on the ambient wind speed near the downwind building, compared to that near the upwind building (Fig. 11c). In addition to the turbulent kinetic energy produced by buoyancy near the heated wall, a large amount of turbulent kinetic energy produced in a shear layer near the roof level is transported to the region near the downwind building wall. By analyzing turbulent kinetic energy fields, it is found that the turbulent kinetic energy produced by wind shear increases with increasing ambient wind speed, but that produced by buoyancy near the heated wall is nearly independent of the ambient wind speed (not shown). Therefore, the sensible heat flux from the downwind building wall in 0800–0900 LST shows a significant

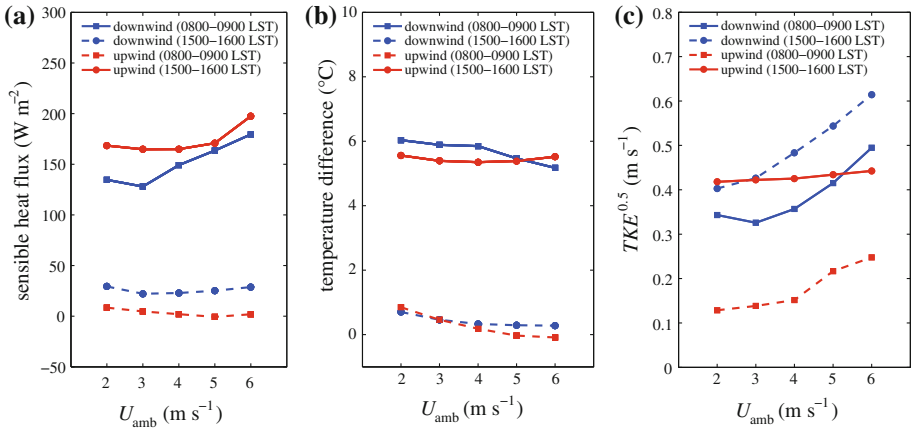

Fig. 11 Variations of hourly averaged **a** surface sensible heat fluxes, **b** temperature differences between walls and adjacent air, and **c** roots of adjacent turbulent kinetic energies (*TKE*) with ambient wind speed. These are for the downwind building wall and upwind building wall in 0800–0900 LST (*square*) and 1500–1600 LST (*circle*). The adjacent air temperatures and the turbulent kinetic energies are *yz*-plane averaged at $x/H = -0.4875$ (the closest plane to the upwind building wall) and $x/H = 0.4875$ (the closest plane to the downwind building wall) in the street canyon

change with the ambient wind speed (from 3 to 6 m s^{-1}), whereas that from the upwind building wall in 1500–1600 LST shows little change with the ambient wind speed (from 2 to 5 m s^{-1}).

The canyon wind speed is primarily related to momentum transport from the ambient flow across a shear layer. In addition, differential sensible heat fluxes from the walls also affect the canyon wind speed. For weak ambient winds, the mean canyon wind speeds in 0800–0900 LST are relatively small because the sensible heat fluxes from the downwind building wall are small. For strong ambient winds, the mean canyon wind speeds in 0800–0900 LST are relatively large because the sensible heat fluxes from the downwind building wall are large. In 1500–1600 LST, however, the mean canyon wind speeds for weak ambient winds are relatively large because the surface sensible heat fluxes for weak ambient winds are still large. This is a reason for large K. Therefore, the different relationships between mean canyon wind speed and ambient wind speed in the two flow regimes are attributed to their different dependencies of surface sensible heat flux on the ambient wind speed.

5 Summary and Conclusions

A CFD model that includes urban surface and radiation processes was developed to investigate the diurnal variation of street-canyon flow. The coupled model predicts surface and substrate temperatures of the roof, walls, and road. When compared to field measurements in summertime, the coupled model well reproduces the diurnal variations of surface temperatures. Flows in a north–south oriented street canyon with $H/W = 1$ were investigated. Two flow regimes in the street canyon are identified by the vortex configuration. Flow regime I characterized by a primary vortex appears for most of the day. Flow regime II characterized by two counter-rotating vortices appears when the downwind building wall is strongly heated in the morning. The street-canyon flow affects the canyon-air temperature field.

The region of cool/warm air appears along the downwind/upwind building wall in flow regime I, whereas it appears in the region of the upper/lower vortex in flow regime II.

The influence of the ambient wind speed on the street-canyon flow is different in the two flow regimes. The extent of the upper/lower vortex in flow regime II expands/shrinks with increasing ambient wind speed and changes the extent of the region of cool/warm air accordingly. On the other hand, the shape of the primary vortex in flow regime I is relatively invariant to the ambient wind speed. Different relationships between mean canyon wind speed and ambient wind speed were found in the two flow regimes. For weak ambient winds, the mean canyon wind speed is relatively small in flow regime II but relatively large in flow regime I. Following the dependency of turbulent kinetic energy on the ambient wind speed near the heated wall, the dependency of surface sensible heat flux on the ambient wind speed is high in flow regime II but low in flow regime I. The dependency of surface sensible heat flux on the ambient wind speed explains the different relationships between mean canyon wind speed and ambient wind speed in the two flow regimes. This can explain the weak intensity of the street-canyon flow in the presence of the downwind building-wall heating, which was found in previous studies (Kim and Baik 1999; Panão et al. 2009).

In our study, the diurnally varying surface temperatures were simulated and used as boundary conditions for the CFD model. This is an essential ingredient in simulating the diurnal variation of street-canyon flow. In our study the calculated surface temperature is a representative temperature for each roof, wall or road surface. For an improved simulation of the diurnally varying street canyon flow, it is necessary to develop a model that is able to calculate the temperature distribution for each surface. Further, pollutant dispersion associated with the diurnally varying street canyon flow deserves investigation.

Acknowledgments The authors are grateful to two anonymous reviewers for providing valuable comments that led to improvements in the original manuscript. This work was funded by the Korea Meteorological Administration Research and Development Program under Grant RACS 2010–4005 and by the Brain Korea 21 Project (through the School of Earth and Environmental Sciences, Seoul National University).

References

Baik JJ, Kang YS, Kim JJ (2007) Modeling reactive pollutant dispersion in an urban street canyon. Atmos Environ 41:934–949

Chen H, Ooka R, Harayama K, Kato S, Li X (2004) Study on outdoor thermal environment of apartment block in Shenzhen, China with coupled simulation of convection, radiation and conduction. Energy Build 36:1247–1258

Cheng WC, Liu CH, Leung DYC (2009) On the correlation of air and pollutant exchange for street canyons in combined wind-buoyancy-driven flow. Atmos Environ 43:3682–3690

Eliasson I, Offerle B, Grimmond CSB, Lindqvist S (2006) Wind fields and turbulence statistics in an urban street canyon. Atmos Environ 40:1–16

Hadavand M, Yaghoubi M, Emdad H (2008) Thermal analysis of vaulted roof. Energy Build 40:265–275

Harman IN, Belcher SE (2006) The surface energy balance and boundary layer over urban street canyons. Q J Roy Meteorol Soc 132:2749–2768

Idczak M, Mestayer P, Rosant JM, Sini JF, Violleau MV (2007) Micrometeorological measurements in a street canyon during the joint ATREUS-PICADA experiment. Boundary-Layer Meteorol 124:25–41

Idczak M, Groleau D, Mestayer P, Rosant JM, Sini JF (2010) An application of the thermo-radiative model SOLENE for the evaluation of street canyon energy balance. Build Environ 45:1262–1275

Kang YS, Baik JJ, Kim JJ (2008) Further studies of flow and reactive pollutant dispersion in a street canyon with bottom heating. Atmos Environ 42:4964–4975

Kim JJ, Baik JJ (1999) A numerical study of thermal effects on flow and pollutant dispersion in urban street canyons. J Appl Meteorol 38:1249–1261

Kim JJ, Baik JJ (2001) Urban street-canyon flows with bottom heating. Atmos Environ 35:3395–3404

Kim JJ, Baik JJ (2004) A numerical study of the effects of ambient wind direction on flow and dispersion in urban street canyons using the RNG k–ε turbulence model. Atmos Environ 38:3039–3048

Kovar-Panskus A, Moulinneuf L, Savory E, Abdelqari A, Sini JF, Rosant JM, Robins A, Toy N (2002) A wind tunnel investigation of the influence of solar-induced wall-heating on the flow regime within a simulated urban street canyon. Water Air Soil Pollut Focus 2:555–571

Lee SH, Park SU (2008) A vegetated urban canopy model for meteorological and environmental modeling. Boundary-Layer Meteorol 126:73–102

Li XX, Liu CH, Leung DYC, Lam KM (2006) Recent progress in CFD modeling of wind field and pollutant transport in street canyons. Atmos Environ 40:5640–5658

Louka P, Vachon G, Sini JF, Mestayer PG, Rosant JM (2002) Thermal effects on the flow in a street canyon—Nantes'99 experimental results and model simulations. Water Air Soil Pollut Focus 2:351–364

Nakamura Y, Oke TR (1988) Wind, temperature and stability conditions in an east-west oriented urban canyon. Atmos Environ 22:2691–2700

Offerle B, Eliasson I, Grimmond CSB, Holmer B (2007) Surface heating in relation to air temperature, wind and turbulence in an urban street canyon. Boundary-Layer Meteorol 122:273–292

Panão MJN, Gonçalves HJP, Ferrão PMC (2007) A matrix approach coupled with Monte Carlo techniques for solving the net radiative balance of the urban block. Boundary-Layer Meteorol 122:217–241

Panão MJN, Gonçalves HJP, Ferrão PMC (2009) Numerical analysis of the street canyon thermal conductance to improve urban design and climate. Build Environ 44:177–187

Ryu YH, Baik JJ, Lee SH (2011) A new single-layer urban canopy model for use in mesoscale atmospheric models. J Appl Meteorol Clim (in press)

Santamouris M, Papanikolaou N, Koronakis I, Livada I, Asimakopoulos D (1999) Thermal and air flow characteristics in a deep pedestrian canyon under hot weather conditions. Atmos Environ 33:4503–4521

Sini JF, Anquetin S, Mestayer PG (1996) Pollutant dispersion and thermal effects in urban street canyons. Atmos Environ 30:2659–2677

Swinbank WC (1963) Long-wave radiation from clear skies. Q J Roy Meteorol Soc 89:339–348

Tsai MY, Chen KS, Wu CH (2005) Three-dimensional modeling of air flow and pollutant dispersion in an urban street canyon with thermal effects. J Air Waste Manag Assoc 55:1178–1189

Uehara K, Murakami S, Oikawa S, Wakanatsu S (2000) Wind tunnel experiments on how thermal stratification affects flow in and above urban street canyons. Atmos Environ 34:1553–1562

Versteeg HK, Malalasekera W (1995) An introduction to computational fluid dynamics: the finite volume method. Longman, Malaysia, 272 pp

Xie X, Huang Z, Wang J, Xie Z (2005) The impact of solar radiation and street layout on pollutant dispersion in street canyon. Build Environ 40:201–212